Research Article | Vol. 31, No. 2 / 16 Jan 2023 / Optics Express 3364
Optics EXPRESS

Lasing modes in ZnO nanowires coupled to planar metals

Daniel Repp,[1,*] Angela Barreda,[1,2] Francesco Vitale,[2] Isabelle Staude,[1,2] Ulf Peschel,[3] Carsten Ronning,[2] and Thomas Pertsch[1,4]

[1]Institute of Applied Physics, Abbe Center of Photonics, Friedrich Schiller University Jena, Albert-Einstein-Straße 15, 07745 Jena, Germany
[2]Institute of Solid State Physics, Friedrich Schiller University Jena, Max-Wien-Platz 1, 07743 Jena, Germany
[3]Institute of Condensed Matter Theory and Solid State Optics, Friedrich Schiller University Jena, Max-Wien-Platz 1, 07743 Jena, Germany
[4]Fraunhofer Institute for Applied Optics and Precision Engineering, Albert-Einstein-Straße 7, 07745 Jena, Germany
*daniel.repp@uni-jena.de

Abstract: Semiconductor nanowire lasers can be subject to modifications of their lasing threshold resulting from a variation of their environment. A promising choice is to use metallic substrates to gain access to low-volume Surface-Plasmon-Polariton (SPP) modes. We introduce a simple, yet quantitatively precise model that can serve to describe mode competition in nanowire lasers on metallic substrates. We show that an aluminum substrate can decrease the lasing threshold for ZnO nanowire lasers while for a silver substrate, the threshold increases compared with a dielectric substrate. Generalizing from these findings, we make predictions describing the interaction between planar metals and semiconductor nanowires, which allow to guide future improvements of highly-integrated laser sources.

1. Introduction

Semiconductor nanowires have attracted a broad interest in recent years and have been studied in fields as diverse as nanosensing [1], nanoscale optoelectronics [2] and thermoelectrics [3]. They are of particular interest in the field of nanophotonics, as they are wavelength-scale nanolasers [4,5].

Nanowire-based lasers form a cylindrical, quasi-one-dimensional cavity and have geometrical extents close to or below optical wavelengths. Since the fabrication of integrated Bragg-reflectors during nanowire growth is challenging at the nanoscale [6], the cavity feedback is often restricted to the back-reflection of the end facets. Furthermore, the lasing properties of nanolasers can be changed by interaction with the substrate. For example, the radiation emitted by the nanowire can interact with the free electron plasma of metallic substrates, forming SPPs [7], [8], which can facilitate a reduction of the mode volume [9].

The reduced mode volume (V) leads to a faster emission dynamics via the Purcell effect [10], which is quantitatively described by the Purcell factor F [11]:

$$F = \frac{\gamma}{\gamma_0} = \frac{3\lambda^3}{4\pi^2}\frac{Q}{V}, \tag{1}$$

where γ is the emission rate of a recombining electron-hole pair in the structure of interest (here the nanowire on top of the metal), γ_0 is the emission rate of the same electron-hole pair in bulk ZnO, λ is the emission wavelength, Q is the quality factor of the resonance and V is the mode volume. Usually, a small dielectric spacer is sandwiched between the nanowire and the metal to

#480742 https://doi.org/10.1364/OE.480742
Journal © 2023 Received 14 Nov 2022; revised 17 Dec 2022; accepted 19 Dec 2022; published 13 Jan 2023

Optics EXPRESS

protect the nanowire emission from quenching by the metal [12]. An illustration of the entire structure can be seen in Fig. 1. The Purcell effect, which is applicable to emission of radiation in general, is discussed in many different lasing applications [13,14]. In fact, the system described above (nanowire on a metallic substrate) is often called a spaser, which is an acronym for "Surface Plasmon Amplification via Stimulated Emission of Radiation", in analogy to the laser [15]. The physical principle of a spaser is equivalent to that of a laser, only the amplified bosonic mode is a surface plasmon polariton instead of a photon [16].

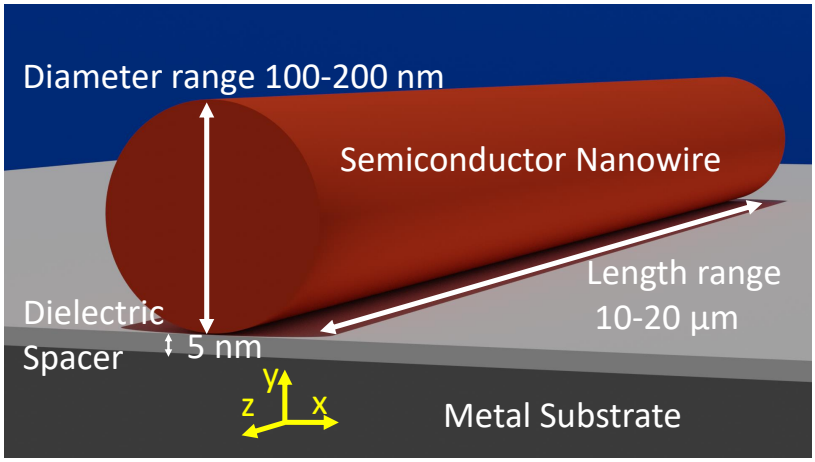

Fig. 1. Scheme of the system under investigation in this article (not to scale). The coordinate system used throughout this article as well as typical geometrical scales are indicated.

In terms of applications, a spaser as described above can be used in the field of biosensing, where nanowire-based sensors have been proven [17]. For this application, there is particular interest in the ultraviolet (UV) spectral range of emission [18] and in metal-enhanced methods [19], making progress in the understanding and optimization of spasers worthwhile.

An interesting semiconductor material for studying the spaser paradigm in the UV spectral range turns out to be Zinc-Oxide (ZnO) because of its high exciton binding energy, supporting excitonic emission and electron-hole-plasma formation even at room temperature [20]. ZnO has a bandgap in the UV spectral range corresponding to an emission wavelength $\lambda \approx$ 380 nm. Interesting metal substrates showing plasma frequencies in this spectral range are silver (Ag) and aluminum (Al) [21]. These two substrates also serve as representative limiting cases for the investigation of plasmonic lasing, since their plasma frequencies are either close to (Ag) or much higher (Al) than the ZnO emission wavelength. In fact, plasmonic lasing has been shown for ZnO nanowires coupled to silver substrates [22], but the lasing thresholds were high due to high propagation losses of the excited SPPs at the emission wavelength of ZnO. Aluminum, on the other hand, offers increased SPP propagation lengths at the ZnO emission wavelength and should therefore also have reduced lasing thresholds if modes strongly coupled to SPPs can be excited. Consequently, it is an interesting question to study the influence of different metallic substrates on the lasing process in semiconductor nanowire lasers, and particularly their lasing thresholds, with ZnO as an interesting and relevant example system. The results presented can easily be transferred to other wavelength regimes and material platforms. Furthermore, a simplified model that treats the dominant processes comprehensively and can predict the structure of lasing modes as a function of several system parameters is of great use for gaining fundamental understanding of the plasmonic lasing process and can guide further design and research decisions. This article provides such a method.

Optics EXPRESS

In this article, a thorough investigation of the influence of nanowire size and substrate material on the Purcell factor is presented. This information is combined with detailed mode calculations and used in a lasing model to determine mode-specific lasing thresholds and thereby quantify mode competition in the system. As a result, we gain fundamental, non-trivial insights into the mode competition processes for ZnO nanowire lasers coupled to planar metals and highlight trade-offs that have to be considered in device design. Furthermore, we provide a versatile, quantitative tool for the description, investigation and optimization of semiconductor lasers in the spaser geometry. Also, we define two coupling regimes between SPPs and nanowire emission, having distinct advantages and disadvantages.

2. Numerical methods

2.1. Mode calculation

An important part of the quantitative description of the lasing process is the proper characterization of the lasing modes regarding critical parameters like propagation losses and gain overlap. The MODE package of the Lumerical software suite was used in order to obtain the transversal eigenmodes of the simulated structures [23]. This package implements an EigenMode Expansion (EME) on a Yee-grid. The rectangular Yee grid is known to lose accuracy for metal interfaces and curved surfaces, both of which are present in our system. Treating the system therefore often requires very fine grids. In order to obtain highly accurate results, a technique called "Conformal Meshing" is used, which calculates effective permittivities close to interfaces and greatly reduces the computational costs.

To correctly connect the Purcell factor and the different mode profiles, a normalization procedure of the modes has to be chosen. The Purcell factor describes the modification of emission rates as a result of changes in the environment. In quantum mechanics, Fermi's Golden rule describes the rate of decay and, correspondingly, photon emission. The matrix element responsible for the description of decay process in Fermi's Golden rule, however, is proportional to the field amplitude. Therefore, a normalization with respect to the field strength has to be chosen, which is defined as

$$\int_A \sum_j |E_{i,j}(\mathbf{r})|^2 = 1, \tag{2}$$

where A is the cross-section through the nanowire center (x-y-plane containing the center of the nanowire) and normal to the nanowire axis (z-axis). $E_{i,j}(\mathbf{r})$ is the j component of the electric field of mode i at position $\mathbf{r}$.

The profiles of some of the transversal modes have been simulated and are plotted in Fig. 2. They are similar to the ones described in Ref. [24]. The plots include the nanowire, the metallic substrate and a dielectric spacer in between. We call the nanowire bound mode with a strong maximum in the nanowire center, and almost no visible interaction with the metal, a "photonic mode", as plotted in Fig. 2(a).

The main interest of this investigation is however on highly confined "plasmonic" modes. These modes exhibit a very small mode volume which leads to a large Purcell factor. The fields of plasmonic modes are mainly confined within the spacer, as shown in Fig. 2(b).

A third "hybrid" mode consists of a nanowire waveguide mode, which is dominantly polarized orthogonally to the metallic substrate. Compared to the plasmonic mode, the overlap with the nanowire material is increased. An example is plotted in Fig. 2(c).

2.2. Purcell factor determination

The Purcell factor was determined by performing Finite-Difference-Time-Domain (FDTD) simulations [23], utilizing a dipole source placed at points inside the nanowire, which maximize the coupling to the modes described in Sec. 2.1. To characterize the photonic mode, the dipole

Optics EXPRESS

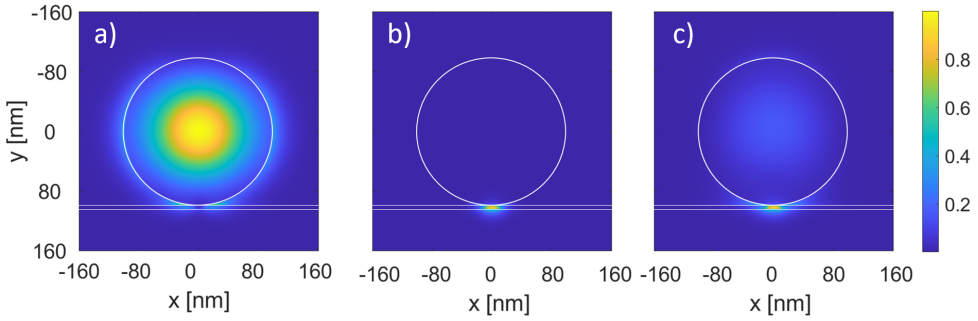

Fig. 2. Example plots of $|E|^2$ of the considered modes for a ZnO nanowire of a diameter of 190 nm on top of a silver substrate with an interposed silica nanometric spacer. Plotted are the a) photonic mode ($n_{\text{eff}} = 2.099 + 0.003i$), b) plasmonic mode ($n_{\text{eff}} = 3.801 + 1.767i$) and c) hybrid mode ($n_{\text{eff}} = 2.073 + 0.02i$).

was placed at the nanowire center. For the plasmonic and hybrid modes, the dipole was placed closely to the metal. Its emission wavelength was set to $\lambda =$ 380 nm, which corresponds to the bandgap of ZnO.

The **E** and **H** fields emitted by the dipole were recorded on the six sides of a small cube (side length of 5 nm) placed around the emitter. The Fourier-transforms of the recorded fields were subsequently used to obtain the spectrum of Poynting vectors, which was integrated over all sides of the cube, yielding the spectral power distribution [25]:

$$P(\omega) = \frac{1}{2}\int_{\text{Box}} Re(\mathbf{E}(\omega) \times \mathbf{H}^*(\omega))d\mathbf{n}, \tag{3}$$

where $d\mathbf{n}$ refers to the surface normal vector perpendicular to each side of the cube. This distribution was subsequently normalized to the injected source power, yielding the Purcell factors F_j by arguments presented in Supplement 1, Sec. 1.A, where j indicates the dipole orientation.

To attribute the Purcel factor calculated at position $\mathbf{r}$ to a specific mode i, the normalized mode profiles $\mathbf{E}_i(\mathbf{r})$ are used. At position $\mathbf{r}$ and with orientation j, the Purcell factor attributed to mode i was calculated as

$$F_{i,j}(\mathbf{r}) = F_j(\mathbf{r}) \cdot \frac{|E_{i,j}(\mathbf{r})|^2}{\Sigma_l |E_{l,j}(\mathbf{r})|^2}, \tag{4}$$

where the index l runs over all modes.

The Purcell factor, as defined above, is a vectorial quantity. To describe the Purcell factor attributable to mode i as a scalar value in a rate-equation model, the stochastic distribution of dipole orientations has to be taken into account. Assuming the electron-hole plasma responsible for gain in ZnO nanowire lasers to be isotropic, the dipole orientation was considered equally distributed, leading to a simple averaging procedure [26]:

$$F_i(\mathbf{r}) = \frac{\sum_j F_{i,j}(\mathbf{r})}{3} \tag{5}$$

where j indicates the dipole orientation.

The nanowire was modeled as an isotropic, non-dispersive dielectric material with a refractive index of 2.5 to conform to the conditions at the emission wavelength of $\lambda =$ 380 nm. The chosen refractive index value corresponds approximately to the value of the refractive index of crystalline ZnO from Ref. [27] and is supported by a calculation from Ref. [28] at the Mott

Optics EXPRESS

density $N_{\mathrm{Mott}} = 2 \cdot 10^{24}\mathrm{m}^{-3}$ (value from [29]), as can be seen also in Ref. [30]. The actual value is seen to vary within a 10-20% range, which is an effect we neglected to keep the model simple. The possible errors caused by this particular choice are elaborated on in Sec. 2.4 and in Supplement 1, Sec. 2.D. The imaginary part of the refractive index was set to zero, as losses and gain are incorporated into the gain profile in the lasing model (see Sec. 2.3).

The nanowire was placed on top of a small silica spacer-layer, which separates the nanowire from a 100 nm thick metal layer, with the metal being either aluminum or silver. Silica was chosen as spacer material since its refractive index is representative for spasers already investigated in practice [5,31,32]. The spacer thickness has been chosen as 5 nm, which is in the range that has been observed as optimal for plasmonic lasing [33,34]. Furthermore, the simulation domain was discretized with a uniform mesh of 1 nm to guarantee the convergence of the results. This discretization is already very fine and prohibits simulating smaller spacer layers. A further reduction of the spacer thickness would result in a divergence of the obtained fields, since the discretization can no longer resolve the fields' spatial dependence. Perfectly Matched Layer (PML) boundary conditions were applied to avoid reflections on the domain boundaries. Both nanowire end facets as well as the metal were extended into the PML to disable end facet reflections, which effectively corresponds to an infinitely long nanowire. Reflections at the nanowire end facets were addressed with a separate FDTD calculation (see Supplement 1, Sec. 2.B).

2.3. Lasing model

A multimode rate-equation lasing model, adapted from Ref. [35], was used to describes the lasing process. Here, a pumping rate P describes optical excitation of charge carriers. After the relaxation of charge carriers, they recombine and emit photons, which couple to specific modes i as described by the Purcell factors F_i calculated above. The rate equations governing the evolution of the charge carrier density n as well as the photon densities s_i in the three competing modes as shown in Fig. 2 are:

$$\begin{aligned}\frac{\mathrm{d}n}{\mathrm{d}t} = \eta\frac{P}{\hbar\omega V_{\mathrm{a}}} - \frac{n}{\tau_{\mathrm{nr}}} - (F_1\beta_1 + F_2\beta_2 + F_3\beta_3)\frac{n}{\tau_{\mathrm{sp}}} \\ - \nu_{\mathrm{g,a}}g(n)(\Gamma_1F_1s_1 + \Gamma_2F_2s_2 + \Gamma_3F_3s_3)\end{aligned} \tag{6}$$

$$\frac{\mathrm{d}s_1}{\mathrm{d}t} = F_1\beta_1\frac{n}{\tau_{\mathrm{sp}}} + \nu_{\mathrm{g,a}}g(n)\Gamma_1F_1s_1 - \frac{s_1}{\tau_{\mathrm{p,1}}} \tag{7}$$

$$\frac{\mathrm{d}s_2}{\mathrm{d}t} = F_2\beta_2\frac{n}{\tau_{\mathrm{sp}}} + \nu_{\mathrm{g,a}}g(n)\Gamma_2F_2s_2 - \frac{s_2}{\tau_{\mathrm{p,2}}} \tag{8}$$

$$\frac{\mathrm{d}s_3}{\mathrm{d}t} = F_3\beta_3\frac{n}{\tau_{\mathrm{sp}}} + \nu_{\mathrm{g,a}}g(n)\Gamma_3F_3s_3 - \frac{s_3}{\tau_{\mathrm{p,3}}}. \tag{9}$$

In this model, η is the absorption efficiency of the optical pump, which is set to 1 to model efficient one-photon above-bandgap excitation, P is the pumping rate, $\hbar$ is the reduced Planck constant, ω is the incoming photon angular frequency and V_{nw} is the volume of the nanowire, which serves as the active medium. $1/\tau_{\mathrm{nr}}$ is the nonradiative decay rate. We kept this rate constant, thereby neglecting higher order nonradiative recombination processes like Auger recombination, to simplify the model. $1/\tau_{\mathrm{sp}}$ is the rate of spontaneous emission. The exciton lifetime τ_{total} in ZnO nanowire is in the range of 200-300 ps [36,37], combining radiative (τ_{sp}) and non-radiative (τ_{nr}) lifetime. Measurements of the Internal Quantum Efficiency (IQE) yield values close to 50%

Optics EXPRESS

[38]. Therefore, we assume that $\tau_{sp} = \tau_{nr}$, resulting in

$$\frac{1}{\tau_{total}} = \frac{1}{\tau_{sp}} + \frac{1}{\tau_{nr}} \tag{10}$$

$$= \frac{2}{\tau_{sp}}, \tag{11}$$

which yields $\tau_{sp} = \tau_{nr} = 2\tau_{total} = 700$ ps. The confinement factors Γ_i were defined as

$$\Gamma_i = \frac{\int_{V_{nw}} \epsilon(\mathbf{r})|E_i(\mathbf{r})|^2}{\int_V \epsilon(\mathbf{r})|E_i(\mathbf{r})|^2} \tag{12}$$

$$\approx \frac{\int_{A_{nw}} \epsilon(\mathbf{r})|E_i(\mathbf{r})|^2}{\int_A \epsilon(\mathbf{r})|E_i(\mathbf{r})|^2}, \tag{13}$$

where V refers to the volume of the entire simulation domain and V_{nw} over the active volume providing the gain for the lasing process, in this case being the nanowire. Furthermore, $\epsilon(\mathbf{r})$ is the permittivity distribution in the simulation domain and $\mathbf{E}_i(\mathbf{r})$ the field profile of mode i. The integration along the nanowire axis cancels out because of translation symmetry, leaving the actual integration to be performed on the nanowire cross section A_{nw} and the cross section of the simulation domain A. There is a slight error caused by the termination of the nanowire which decreases with increasing nanowire length. This expression, although not accurate for open systems, leads to reliable results. Special care is necessary for open systems, which can be treated by quasi-normal modes [39].

Note that, while Γ_i is calculated for the entire simulation domain, the value is dominated by the maximum of the specific mode. Even more so because of the high value of the nanowire permittivity. This justifies the connection of a confinement factor Γ_i and a Purcell factor F_i calculated for only one dipole position.

Also, note that the fraction of spontaneous emission into mode i was chosen as $\beta_i = \frac{\Gamma_i}{\Gamma_1+\Gamma_2+\Gamma_3}$. This choice is a sum over all longitudinal cavity modes in the nanowire having the same transversal mode profile. It neglects all other modes except for the ones considered, as well as emission in free space, and weights the amount of spontaneous emission into mode i by its overlap with the gain material. Note that this is a heuristic approach motivated by Ref. [40].

Furthermore, the medium group velocity is defined as

$$v_{g,a} = \frac{c}{\frac{d(\omega n')}{d\omega}}, \tag{14}$$

with n' being the active medium refractive index, and $g(n)$ is the active medium gain as in [35], given by

$$g(n) = g_0 \ln(\frac{n}{n_{tr}}), \tag{15}$$

with $n_{tr} = N_{Mott} = 2 \cdot 10^{24} m^3$ the transparency density, which we set equal to the Mott density for formation of an electron-hole plasma [28]. The transparency density changes with wavelength, but the Mott density gives a good order-of-magnitude estimate. Furthermore, we set $g_0 = 0.7\ \mu m^{-1}$ [41].

The modal losses are modelled via a loss rate, given by

$$\frac{1}{\tau_{p,i}} = v_{gz,i}\left(\alpha_i + \frac{1}{2L}\ln(\frac{1}{R_i^2}),\right) \tag{16}$$

where $v_{gz,i} = c/n_i'$, with n_i' being the mode group index, is the mode group velocity, α_i is the modal propagation loss (see Supplement 1, Sec. 2.A), L the length of the nanowire (we set $L = 10\ \mu m$) and R_i the end facet reflectivity for mode i (see Supplement 1, Sec. 2.B).

Optics EXPRESS

2.4. Thresholds

To identify the lasing threshold, the initial value problem defined by the lasing model was solved using an implicit multi-step Runge-Kutta time-stepping algorithm, implemented in the Python SciPy package. The initial charge carrier density was set to $1\mathrm{m}^{-3}$ to treat an ideal, defect-free semiconductor without intrinsic doping while avoiding a diverging logarithm. The initial photon densities were set to $0\mathrm{m}^{-3}$. The simulation time was set to 10 ns, but the results do not depend on the simulation time in a window of 100 ps to 10 ns.

Sweeps of the pumping rate P were performed until characteristic relaxation oscillations of the photon number are observed, which are identified by comparing the maximum and steady-state values of the photon numbers in the time trace. If they differed by more than 10%, the corresponding power is defined as the threshold power, and subsequently divided by the area of a circular laser spot size of 10 μm to obtain the intensity.

The nanowire material model has an impact on the accuracy of the threshold calculation, since the chosen refractive index is on the upper end of the likely values and changes during the build-up of the electron-hole plasma. First of all, it overestimates the end facet reflectivity, leading to an underestimation of the thresholds, particularly of the photonic modes. On the other hand, it also underestimates the Purcell factor of plasmonic/hybrid modes, leading to an overestimation of the threshold. These effects cause a correction of the results, but can be incorporated into the model by a careful, piecewise modeling of the loss channels. Detailed plots showing these error sources can be found in Supplement 1, Sec 2.D.

2.5. FDTD lasing calculations

Additionally to the model presented in Sec. 2.3, full-wave FDTD calculations were performed for selected nanowire diameters in order to corroborate the developed approximative lasing model.

The gain model used was the 4-level-2-electron material with a pumping level at 350 nm (FWHM 0.8 nm) and a broad lasing level at 380 nm (FWHM 8 nm). The nanowire was pumped via mode-sources [23] oriented perpendicular to the nanowire axis. We solve for the transversal eigenmodes (plasmonic, photononic, and hybrid modes) and excite these modes simultaneously with an equal amplitude of $10^3 \cdot \mathrm{V\,m}^{-1}$ and a broadband excitation source centered at λ = 380 nm with a pulse bandwidth of 100 nm, thereby spanning the whole lasing gain spectrum approximately uniformly and resulting in a pulse duration of approximately 2 fs.

The spatial and spectral field distribution of the emitted pulse is recorded via 10 power monitors transversal to the nanowire axis, separated by 50 nm. The inversion of the lasing level is increased until the power through the power monitors shows peaks, being characteristic of lasing. This happens at an inversion of 0.1 for aluminum and 0.2 for silver. At the wavelength showing maximum power transmitted through the monitor, the spatial field distribution is analyzed.

3. Results and discussion

3.1. Lasing of nanowires on a dielectric substrate

The lasing model described above was first applied to a nanowire placed on top of a silica substrate. In Sec. 3.3., these results were compared with those obtained considering the nanowire to be placed on metallic substrates, separated by a thin dielectric spacer.

Mode characterization: The nanowire diameter is varied between 120 nm and 190 nm in steps of 10 nm to characterize size-dependent effects. This diameter range was chosen because the photonic mode is expected to be mainly responsible for lasing in this regime for a silica substrate, since the modes shown in 2(b,c) cannot exist because of the lack of plasmonic confinement. It also includes the range at which the photonic mode loses support via leakage into free space and thereby is interesting in terms of mode competition with plasmonic modes, which lack this cut-off. Since for diameters below 120 nm, no nanowire-bound modes could be found, the analysis starts

Optics EXPRESS

at 120 nm. The upper end of this range was chosen because for diameters larger than 190 nm, higher-order modes appear, which complicate the calculation process while not leading to an improvement of the description of competition with plasmonic modes.

As can be seen in Fig. 3, the overlap with the gain material decreases with decreasing diameter, as the mode loses confinement at small diameters. The modal loss rate, on the other hand, increases, as the end facet reflectivity decreases as a consequence of mode leakage into the environment and free space.

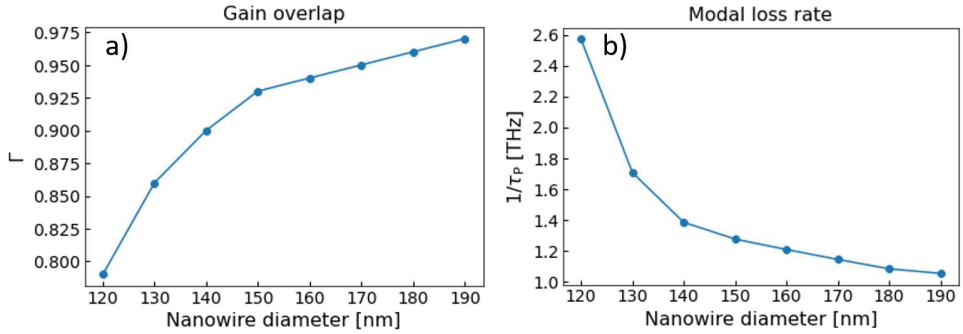

Fig. 3. a) Gain overlap and b) modal loss rate for the photonic mode of a ZnO nanowire placed on a silica substrate as a function of the nanowire diameter.

Purcell factor: The results of the Purcell factor calculation as described in Sec. 2.2 can be found in Fig. 4(a). The dipole was placed in the nanowire center, where the maximum of the photonic mode is located. The Purcell factor of the photonic mode drops with decreasing diameter as the mode increasingly leaks into the environment, thereby increasing the mode area.

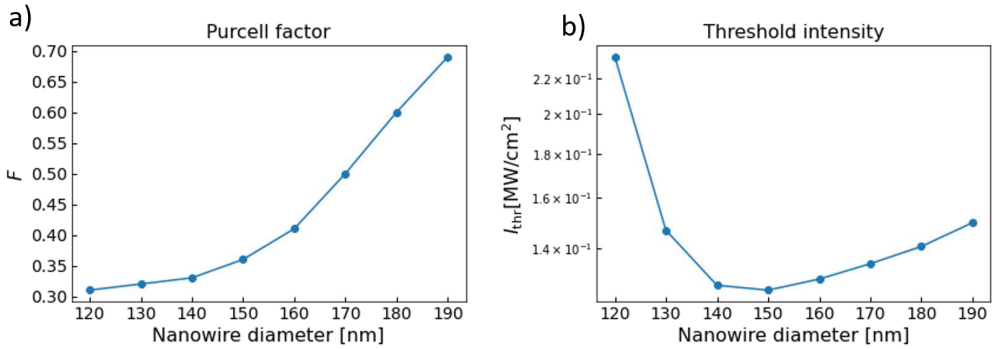

Fig. 4. a) Purcell factor for a dipole decaying at the nanowire center as a function of the nanowire diameter. b) Threshold intensity as a function of nanowire diameter.

Lasing threshold calculation: The threshold intensity, which is plotted in Fig. 4(b), depends on the nanowire diameter. The threshold first decreases with decreasing diameter as a result of the fact that with smaller nanowires, less material loss needs to be compensated. The threshold reaches a minimum around 150 nm and increases again for further decreasing diameters since the photonic mode increasingly leaks into the surrounding medium.

3.2. Dipole position for metallic substrates

Turning towards metallic substrates, aluminum and silver are identified as the most interesting substrates as they feature plasma frequencies in the UV spectral range. While the former

Optics EXPRESS

has a plasma frequency corresponding to a wavelength of 80 nm, the latter has a plasma frequency corresponding to a wavelength of 330 nm. One would therefore expect a much stronger plasmonic enhancement for silver, since its plasma frequency is closer to the emission wavelength ($\lambda = 380$ nm) of ZnO.

An increase of the Purcell factor when moving the dipole closer to the metal is expected, as the interaction with SPPs, which are exponentially confined to the interface between metal and dielectric, becomes stronger. In other words, the SPPs add a contribution to the local density of optical states (LDOS) only accessible for emitters close to the metal. The Purcell factor was analyzed as a function of position and orientation for the two metals for a nanowire with a diameter of 200 nm. While being slightly outside the investigated range of 120 nm -190 nm, the Purcell factor values quantitatively agree with the values found when the calculation is repeated for a nanowire of diameter 190 nm, as is shown in Supplement 1, Sec. 2.E. Choosing a large diameter has the advantages of small mode leakage into free space and a large spatial separation between the maxima of the considered modes. The dipole position is parameterized in terms of the "Dipole offset", defined as the distance between dipole and the top of the dielectric spacer. The requirement of having at least one mesh cell between the dipole box walls and the emitter as well as having no material change inside the box leads to the minimum achievable distance between spacer and dipole of 5 nm, given a uniform mesh with a 1 nm discretization.

Figure 5 shows an increase of the Purcell factors for a polarization perpendicular to the metal surface (here y) when approaching the aluminum substrate and for all polarizations on the silver substrate. The y-polarization is dominant with respect to the plasmonic enhancement because plasmons are mainly polarized in the y-direction.

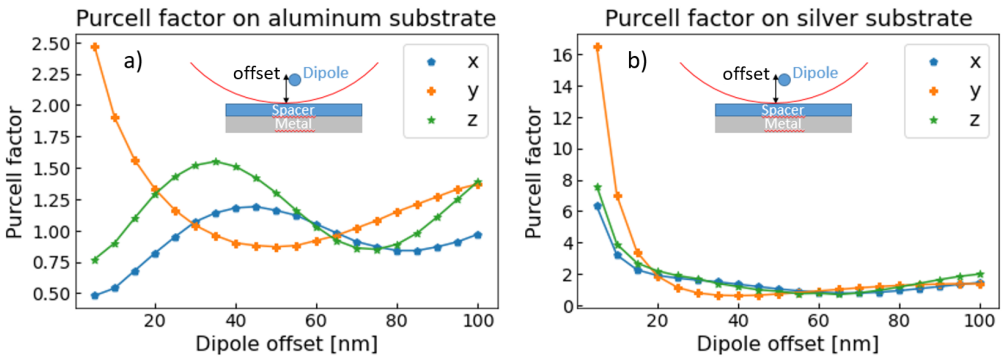

Fig. 5. Purcell factor as a function of dipole position relative to nanowire-spacer interface (offset) for an a) aluminum and a b) silver substrate.

The fact that the Purcell factor increases for all polarization directions on silver as compared to only one on aluminum might be related to a closer match to the plasma frequency for silver, leading to a larger degree of confinement in the metal plane for the silver SPPs. The high plasma frequency of aluminum, on the other hand, leads to its behavior as "perfect metal" or "perfect mirror", thereby suppressing electric field components parallel to the metal plane. Correspondingly, the modes close to the surface become mostly y-polarized. To fulfill the divergence condition in Maxwell's equations

$$\nabla \cdot \boldsymbol{E} \approx \frac{\partial E_y}{\partial y} = 0, \tag{17}$$

E_y can only vary weakly in the y-direction, thus spreading the mode towards the center of the nanowire, reducing the plasmonic confinement and reducing the Purcell factor overall.

Optics EXPRESS

In the following, when calculating the Purcell factors of the plasmonic as well as the hybrid mode, the dipole is placed as close as possible to the metal. To be more precise, the offset as defined in Fig. 5, is fixed at 5 nm. Within numerical accuracy, this corresponds to the maximum of the plasmonic and hybrid mode within the nanowire. For calculating the Purcell factor of the photonic mode, the dipole is still put in the nanowire center. Additionally, for both positions, we performed a sweep of the nanowire refractive index for the out-of-plane (z-) electric field component for a nanowire on a silver substrate and in air, further supporting our hypothesis that emitters in the nanowire center do not couple to plasmonic modes. The results are shown in Supplement 1, Sec. 2.F.

3.3. *Lasing of nanowires on plasmonic substrates*

3.3.1. Aluminum substrate

Mode characterization: The gain overlap Γ and the modal loss rate $1/\tau_p$ were analyzed, as can be seen in Fig. 6 and compared with the case of a silica substrate. The gain overlap (Fig. 6(a)) is reduced for the plasmonic mode, but it is still significant. This is due to the high permittivity of ZnO, which is used for "weighting" the field distribution (see Eq. (13)). The photonic mode on aluminum shows a slightly higher gain overlap than the one on silica, since leakage into the substrate is reduced.

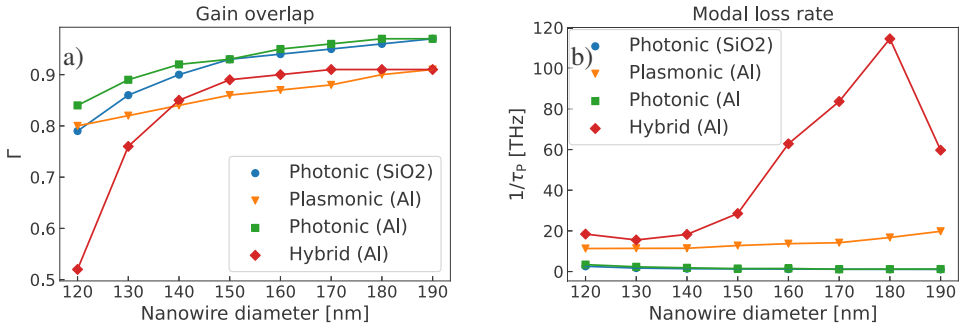

Fig. 6. a) Gain overlap and b) modal loss rate for the three modes of a nanowire placed on an aluminum substrate and the mode on a silica substrate as a function of nanowire diameter.

For large diameters, the hybrid mode has overlap values between the photonic and the plasmonic mode, as is expected, given its hybrid character. For smaller diameters, the hybrid mode cuts-off faster than the photonic mode, and therefore has a reduced gain overlap.

The modal loss rate (Fig. 6(b)) of the plasmonic mode and the hybrid mode are increased strongly with respect to the photonic modes, which is mainly a result of the non-negligible propagation losses, and decreases with decreasing diameter. Interestingly, the modal loss rate of the hybrid mode reaches a value as high as ca. 115 THz at about 180 nm. This is caused by high propagation losses and a high modal group velocity around this point (see Supplement 1, Sec. 2.C).

Purcell factor: Another influence of the aluminum substrate is a modification of the Purcell factor. To characterize the Purcell factors of the three modes, in separate simulations, one dipole is placed in the center of the nanowire and one at the bottom. The Purcell factors $F_{x,y,z}$ were calculated and averaged as in Sec. 3.1. In Fig. 7(a), it is shown that the Purcell factor of the photonic mode is reduced for the aluminum substrate, which supports more modes that compete for gain.

Interestingly, the hybrid mode as well as the plasmonic mode have an increased Purcell factor. But while the hybrid mode dominates at large diameters, the plasmonic mode dominates at small diameters, whereas the hybrid mode cuts off at small diameters.

Optics EXPRESS

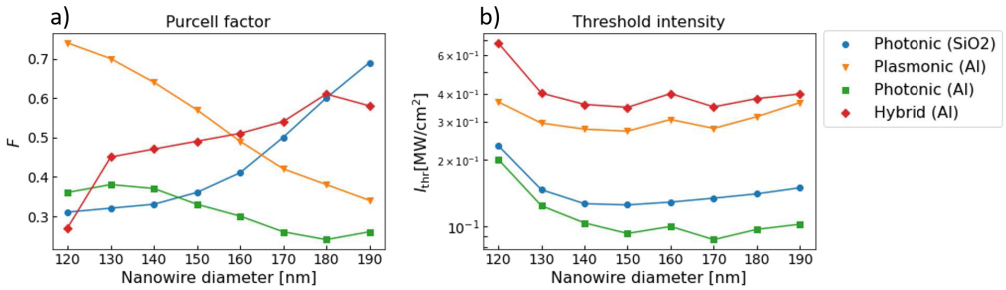

Fig. 7. a) Purcell factor for a dipole decaying at the nanowire bottom (plasmonic & hybrid modes) and the nanowire center (photonic modes for both substrates) as a function of the nanowire diameter. b) Threshold intensity of the modes under consideration as a function of nanowire diameter.

Lasing threshold calculation: The threshold intensities of all three modes were calculated and compared with the threshold intensity on a silica substrate in Fig. 7(b). The plasmonic mode and the hybrid mode on the aluminum substrate have the highest thresholds. The threshold depends on the nanowire diameter, as expected from their weak degree of confinement to the spacer.

The photonic modes have similar thresholds in the small diameter range independently of the substrate. Remarkably, for larger diameters, the aluminum substrate leads to a threshold reduction, since leakage into the substrate is reduced, but effectively no coupling to highly dissipative SPPs is taking place.

We conclude that on aluminum, the photonic mode dominates the lasing process under steady-state conditions. The losses of the plasmonic and the hybrid mode cannot be compensated by the increased Purcell factor.

3.3.2. Silver substrate

In contrast to the case of the aluminum substrate, the high losses of silver in the UV spectral range of interest prevent the possibility of pure plasmonic lasing with field distributions as shown in Fig. 2(b). For example, for a nanowire diameter of 120 nm, the photonic mode effective refractive index has an imaginary part of 0.009 and the hybrid mode 0.3, whereas the plasmonic mode effective refractive index has an imaginary part of 1.67. Therefore, we only consider the photonic and the hybrid modes. Note, however, that hybrid modes, as sketched in Fig. 2(c), also lead to the excitation of plasmons, but suffer smaller losses.

Mode characterization: The modes could only be clearly distinguished starting at 130 nm. The photonic modes have a similar overlap with the gain material, as can be seen in Fig. 8(a). The hybrid mode, on the other hand, has an increased overlap with the gain medium caused by the field enhancement close to the metal. The modal loss rates (Fig. 8(b)) for both modes are increased significantly compared to the photonic mode on a silica substrate. Furthermore, the losses of both modes increase with decreasing diameter because the mode fraction overlapping with the gain material leaks into free space.

Purcell factor calculation: The Purcell factors are much smaller than expected from Fig. 5(b), since most of the high Purcell factor is attributed to the highly damped plasmonic mode. The Purcell factor of the hybrid mode is small for high diameters, but increases at lower diameters, as can be seen in Fig. 9(a).

Lasing threshold calculation: The threshold intensities plotted in Fig. 9(b) show a large increase overall and with respect to the nanowire diameter. For almost all but very high diameters, the hybrid mode will dominate the lasing process.

Optics EXPRESS

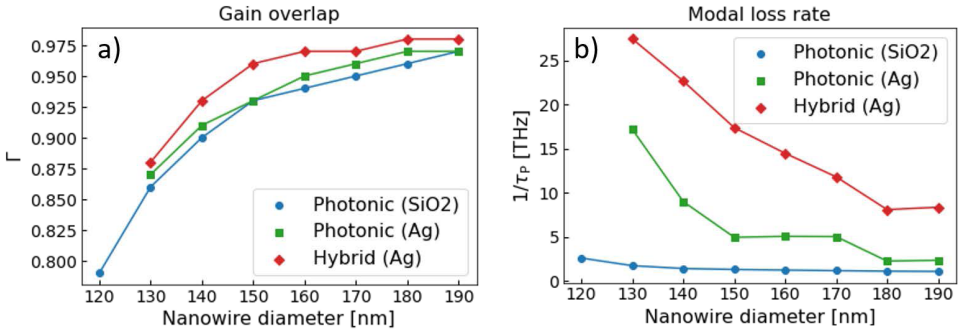

Fig. 8. a) Gain overlap and b) modal loss rate for the two modes of a nanowire placed on a silver substrate and the mode on a silica substrate as a function of the nanowire diameter.

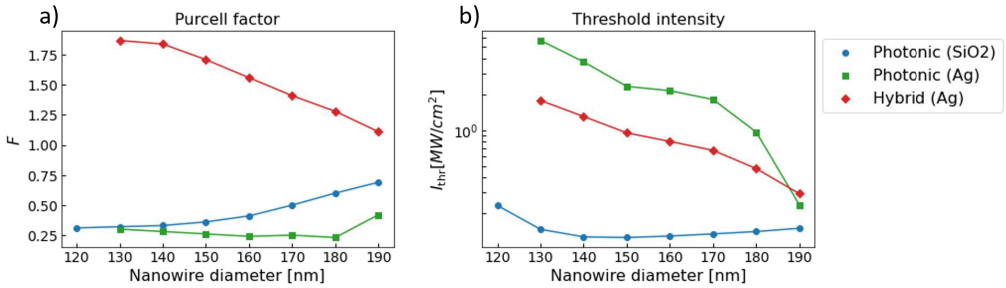

Fig. 9. a) Purcell factor for a dipole decaying at the nanowire bottom (hybrid mode) and the nanowire center (photonic modes for both substrates) as a function of the nanowire diameter for a silver substrate. b) Threshold intensities of the modes under consideration as a function of nanowire diameter.

Note that these results offer a new perspective for the interpretation of previously published results [5]. A careful analysis of the mode profiles shows that the modes found to be responsible for lasing by Oulton et al. in Ref. [5] on the plasmonic substrate are in fact the "hybrid" modes in our terminology. The order-of-magnitude increase of the lasing threshold below a 100 nm nanowire diameter fits nicely with the cut-off expected for nanowire-bound modes (At around 120 nm diameter, the photonic modes cannot be found in our solver.) and the losses of the purely plasmonic modes (see introductory text for Sec. 3.3.2).

3.3.3. FDTD calculations of field distribution at the lasing wavelength

As explained in Sec. 2.5, FDTD calculations were performed to corroborate the findings presented above. The results of these FDTD calculations for two nanowires with identical diameters and excitation conditions but two different substrates are presented in Fig. 10. Evidently, the field distribution for the case of an aluminum substrate is concentrated inside the nanowire, whereas for a silver substrate, excitation of SPPs close to the metal surface can be observed, while still a strong overlap with the nanowire is present.

One striking result from these calculations is that, even though not seeded directly, a "donut"-mode coexists with the photonic mode. The increased power as measured in the lasing spectrum is mainly caused by the "wedges" at the nanowire bottom. The appearance of this mode points to the fact that higher order modes and transerval spatial hole-burning have to be taken into account at larger diameters for a more complete picture. However, since the donut mode is essentially a higher-order photonic mode, it does not invalidate our conclusion.

Optics EXPRESS

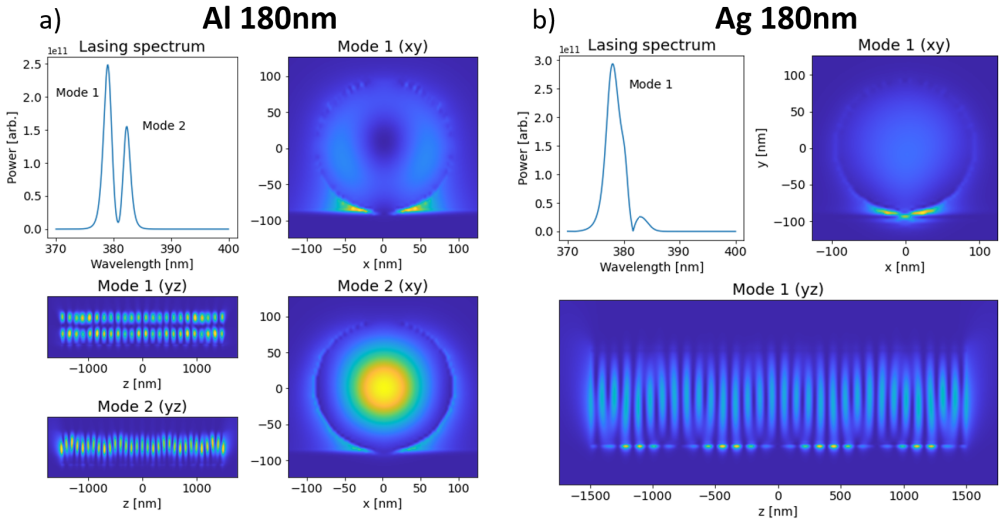

Fig. 10. Distribution of $|E|^2$, normalized to the respective maximum value, in the lasing regime for a ZnO nanowire of diameter 180 nm on top of a) an aluminum substrate and b) a silver substrate. A 5 nm silica spacer was included in both cases.

Together, both calculations show that lasing for a silver substrate is dominated by hybrid modes, whereas for aluminum, little interaction with surface plasmons is taking place.

4. Conclusions

We have set out to quantify the effect of metallic substrates on the lasing thresholds of ZnO nanowire lasers. In the process, we have derived an intuitive method to quantify the effect of plasmonically-induced Purcell factor enhancement on silver and aluminum substrates. We presented detailed mode calculations and a rate-equation model to study mode competition.

Considering silver, a plasmonic material with a plasma frequency being close to the bandgap of ZnO, we have shown that plasmonic lasing is a double-edged sword: On the one hand, the low mode volume of SPP-modes offers interesting possibilities with respect to the strong increase of the Purcell factor. On the other hand, the high propagation losses make an excitation of these modes in a steady-state or quasi-steady-state regime very difficult.

As expected, silver shows a strong effect on lasing properties and even offers the possibility to access hybrid modes in the steady-state by compensating increased losses by increased Purcell factors and gain overlap. Aluminum, on the other hand, does not offer these advantages. But curiously, an aluminum substrate decreases the threshold for photonic lasing as compared to a photonic substrate, since the small penetration depth suppresses mode leakage into the substrate.

These findings should also be valid for other combinations of nanowire materials and metal substrates. We expect for metals with plasma frequencies far above the nanowire bandgap and with nanowire diameters comparable to λ/n, where n is the nanowire refractive index at the emission wavelength, a threshold reduction without plasmon excitation. This is caused by a reduction of leakage into the substrate or, in other words, a small penetration depth into the metal. On the other hand, for resonant combinations, we expect a threshold increase accompanied by excitation of SPPs.

Another interesting finding is related to the polarization properties of emitters close to the substrate. Highly-resonant combinations of nanowire lasing wavelength and plasma frequency

Optics EXPRESS

seem to offer an increase of the emission rate independently of the emitter polarization, whereas in an off-resonant configuration, mainly emitters polarized normal to the metal experience enhancement.

Funding. Deutsche Forschungsgemeinschaft (2675 'Meta-ACTIVE', 437527638, 398816777, CRC 1375).

Acknowledgments. We acknowledge the financial support via the project ID 398816777 in the CRC 1375 "NOA–Nonlinear optics down to atomic scales" funded by the Deutsche Forschungsgemeinschaft (DFG).

A.B. thanks the financial support of the German Research Foundation (DFG) under the framework of the International Research Training Group (IRTG) 2675 "META-ACTIVE".

Disclosures. The authors declare no conflicts of interest.

Data Availability. All relevant modeling data not provided in the main text can be found in the Supplementary document. For all substrates, the propagation losses, the end facet reflectivity and the modal group velocity is provided.

Supplemental document. See Supplement 1 for supporting content.

References

1. R. Röder, T. P. H. Sidiropoulos, R. Buschlinger, M. Riediger, U. Peschel, R. F. Oulton, and C. Ronning, "Mode switching and filtering in nanowire lasers," Nano Lett. **16**(4), 2878–2884 (2016).
2. P.-C. Chang, Z. Fan, C.-J. Chien, D. Stichtenoth, C. Ronning, and J. G. Lu, "High-performance zno nanowire field effect transistors," Appl. Phys. Lett. **89**(13), 133113 (2006).
3. J. Moon, J.-H. Kim, Z. C. Chen, J. Xiang, and R. Chen, "Gate-modulated thermoelectric power factor of hole gas in ge-si core-shell nanowires," Nano Lett. **13**(3), 1196–1202 (2013).
4. S. I. Azzam, A. V. Kildishev, R.-M. Ma, C.-Z. Ning, R. Oulton, V. M. Shalaev, M. I. Stockman, J.-L. Xu, and X. Zhang, "Ten years of spasers and plasmonic nanolasers," Light: Sci. Appl. **9**(1), 90 (2020).
5. R. F. Oulton, V. J. Sorger, T. Zentgraf, R.-M. Ma, C. Gladden, L. Dai, G. Bartal, and X. Zhang, "Plasmon lasers at deep subwavelength scale," Nature **461**(7264), 629–632 (2009).
6. J. B. Wright and I. Brener, "Distributed feedback gallium nitride nanowire lasers," Appl. Phys. Lett. **104**(4), 041107 (2014).
7. K. Okamoto, I. Niki, A. Shvartser, Y. Narukawa, T. Mukai, and A. Scherer, "Surface-plasmon-enhanced light emitters based on ingan quantum wells," Nat. Mater. **3**(9), 601–605 (2004).
8. N. Gao, K. Huang, J. Li, S. Li, X. Yang, and J. Kang, "Surface-plasmon-enhanced deep-uv light emitting diodes based on algan multi-quantum wells," Sci. Rep. **2**(1), 816 (2012).
9. D. J. Bergman and M. I. Stockman, "Surface plasmon amplification by stimulated emission of radiation: quantum generation of coherent surface plasmons in nanosystems," Phys. Rev. Lett. **90**(2), 027402 (2003).
10. Y. Gu, L. Wang, P. Ren, J. Zhang, T. Zhang, O. J. F. Martin, and Q. Gong, "Surface-plasmon-induced modification on the spontaneous emission spectrum via subwavelength-confined anisotropic purcell factor," Nano Lett. **12**(5), 2488–2493 (2012).
11. S. V. Gaponenko, Introduction to Nanophotonics (Cambridge University Press, 2010).
12. Q.-H. Ren, Y. Zhang, H.-L. Lu, H.-Y. Chen, Y. Zhang, D.-H. Li, W.-J. Liu, S.-J. Ding, A.-Q. Jiang, and D. W. Zhang, "Surface-plasmon mediated photoluminescence enhancement of pt-coated ZnO nanowires by inserting an atomic-layer-deposited al2o3spacer layer," Nanotechnology **27**(16), 165705 (2016).
13. C. Walther, G. Scalari, M. Beck, and J. Faist, "Purcell effect in the inductor-capacitor laser," Opt. Lett. **36**(14), 2623–2625 (2011).
14. H. Altug, D. Englund, and J. Vučković, "Ultrafast photonic crystal nanocavity laser," Nat. Phys. **2**(7), 484–488 (2006).
15. M. M. Tohari, A. Lyras, and M. S. AlSalhi, "A novel metal nanoparticles-graphene nanodisks-quantum dots hybrid-system-based spaser," Nanomaterials **10**(3), 416 (2020).
16. M. A. Noginov, G. Zhu, M. Mayy, B. A. Ritzo, N. Noginova, and V. A. Podolskiy, "Stimulated emission of surface plasmon polaritons," Phys. Rev. Lett. **101**(22), 226806 (2008).
17. P. Ambhorkar, Z. Wang, H. Ko, S. Lee, K.-I. Koo, K. Kim, and D.-I. D. Cho, "Nanowire-based biosensors: From growth to applications," Micromachines **9**(12), 679 (2018).
18. B. Kalas, K. Ferencz, A. Saftics, Z. Czigany, M. Fried, and P. Petrik, "Bloch surface waves biosensing in the ultraviolet wavelength range – bragg structure design for investigating protein adsorption by in situ kretschmann-raether ellipsometry," Appl. Surf. Sci. **536**, 147869 (2021).
19. S. M. Fothergill, C. Joyce, and F. Xie, "Metal enhanced fluorescence biosensing: from ultra-violet towards second near-infrared window," Nanoscale **10**(45), 20914–20929 (2018).
20. D. Vanmaekelbergh and L. K. van Vugt, "Zno nanowire lasers," Nanoscale **3**(7), 2783–2800 (2011).
21. D. Gérard and S. K. Gray, "Aluminium plasmonics," J. Phys. D: Appl. Phys. **48**(18), 184001 (2015).
22. T. Sidiropoulos, "Ultrafast plasmonic nanowire lasers near the surface plasmon frequency," Nat. Phys. **10**(11), 870–876 (2014).
23. "Lumerical fdtd solutions," www.lumerical.com. Lumerical Version 2019aR2.

Optics EXPRESS

24. L. Zhu, "Modal properties of hybrid plasmonic waveguides for nanolaser applications," IEEE Photonics Technol. Lett. **22**(8), 535–537 (2010).
25. "Integrating the poynting vector," https://support.lumerical.com/hc/en-us/articles/1500007397442-Integrating-the-Poynting-Vector. Version 2019aR2.
26. T. D. Schmidt, M. Flämmich, B. J. Scholz, D. Michaelis, C. Mayr, N. Danz, and W. Brütting, "Non-isotropic emitter orientation and its implications for efficiency analysis of organic light-emitting diodes," Proc. SPIE **8435**, 843513 (2012).
27. H. Yoshikawa and S. Adachi, "Optical constants of ZnO," Jpn. J. Appl. Phys. **36**(10R), 6237–6243 (1997).
28. M. A. M. Versteegh, "Ultrafast screening and carrier dynamics in zno: Theory and experiment," Phys. Rev. B **84**(3), 035207 (2011).
29. M. A. Versteegh, D. Vanmaekelbergh, and J. I. Dijkhuis, "Lasing in zno nanowires is electron-hole plasma lasing," in *CLEO: 2011 - Laser Science to Photonic Applications*, (2011), pp. 1–2.
30. M. Wille, C. Sturm, T. Michalsky, R. Röder, C. Ronning, R. Schmidt-Grund, and M. Grundmann, "Carrier density driven lasing dynamics in zno nanowires," Nanotechnology **27**(22), 225702 (2016).
31. Y.-H. Chou, Y.-M. Wu, K.-B. Hong, B.-T. Chou, J.-H. Shih, Y.-C. Chung, P.-Y. Chen, T.-R. Lin, C.-C. Lin, S.-D. Lin, and T.-C. Lu, "High-operation-temperature plasmonic nanolasers on single-crystalline aluminum," Nano Lett. **16**(5), 3179–3186 (2016).
32. X. Liu, Q. Zhang, J. N. Yip, Q. Xiong, and T. C. Sum, "Wavelength tunable single nanowire lasers based on surface plasmon polariton enhanced burstein–moss effect," Nano Lett. **13**(11), 5336–5343 (2013).
33. L. Wang, X. Wang, S. Mao, H. Wu, X. Guo, Y. Ji, and X. Han, "Strongly enhanced ultraviolet emission of an au@sio2/zno plasmonic hybrid nanostructure," Nanoscale **8**(7), 4030–4036 (2016).
34. Y.-J. Liao, C.-W. Cheng, B.-H. Wu, C.-Y. Wang, C.-Y. Chen, S. Gwo, and L.-J. Chen, "Low threshold room-temperature uv surface plasmon polariton lasers with zno nanowires on single-crystal aluminum films with al2o3 interlayers," RSC Adv. **9**(24), 13600–13607 (2019).
35. E. Bermúdez-Ureña, G. Tutuncuoglu, J. Cuerda, C. L. C. Smith, J. Bravo-Abad, S. I. Bozhevolnyi, A. Fontcuberta i Morral, F. J. García-Vidal, and R. Quidant, "Plasmonic waveguide-integrated nanowire laser," Nano Lett. **17**(2), 747–754 (2017).
36. J. S. Reparaz, G. Callsen, M. R. Wagner, F. Güell, J. R. Morante, C. M. Sotomayor Torres, and A. Hoffmann, "Spatial mapping of exciton lifetimes in single zno nanowires," APL Mater. **1**(1), 012103 (2013).
37. S. Hong, T. Joo, W. I. Park, Y. H. Jun, and G.-C. Yi, "Time-resolved photoluminescence of the size-controlled zno nanorods," Appl. Phys. Lett. **83**(20), 4157–4159 (2003).
38. D. J. Gargas, H. Gao, H. Wang, and P. Yang, "High quantum efficiency of band-edge emission from zno nanowires," Nano Lett. **11**(9), 3792–3796 (2011).
39. A. F. Koenderink, "On the use of purcell factors for plasmon antennas," Opt. Lett. **35**(24), 4208–4210 (2010).
40. J. Vuckovic, O. J. Painter, Y. Xu, A. Yariv, and A. Scherer, "FDTD calculation of the spontaneous emission coupling factor in optical microcavities," Proc. SPIE **3937**, 2–11 (2000).
41. K. Bohnert, G. Schmieder, and C. Klingshirn, "Gain and reflection spectroscopy and the present understanding of the electron–hole plasma in ii–vi compounds," Phys. Status Solidi B **98**(1), 175–188 (1980).